ACS APPLIED MATERIALS & INTERFACES

Article

Covalent Organic Framework Material bearing Phloroglucinol Building Units as a Potent Anticancer Agent

Piyali Bhanja, Snehasis Mishra, Krishnendu Manna, Arijit Mallick, Krishna Das Saha, and Asim Bhaumik

ACS Appl. Mater. Interfaces, **Just Accepted Manuscript** • DOI: 10.1021/acsami.7b07343 • Publication Date (Web): 23 Aug 2017

Just Accepted

ACS Publications

ACS Applied Materials & Interfaces is published by the American Chemical Society.
1155 Sixteenth Street N.W., Washington, DC 20036

Covalent Organic Framework Material bearing Phloroglucinol Building Units as a Potent Anticancer Agent

Piyali Bhanja,[1,‡] Snehasis Mishra,[2,‡] Krishnendu Manna,[2] Arijit Mallick,[3] Krishna Das Saha[2] and Asim Bhaumik*[,1]

[1]*Department of Materials Science, Indian Association for the Cultivation of Science, Jadavpur, Kolkata – 700 032, India.*

[2]*Cancer & Inflammatory Disorder Division, CSIR-Indian Institute of Chemical Biology, Kolkata - 700032, India.*

[3]*Advanced Membranes and Porous Materials Center, Division of Physical Sciences and Engineering, King Abdullah University of Science and Technology (KAUST), Thuwal 23955-6900, Saudi Arabia..*

ABSTRACT: Covalent organic frameworks (COFs) having periodicity in pores of nanoscale dimensions can be suitably designed for the organic building units bearing reactive functional groups at their surfaces. Thus, they are an attractive option as an anticancer agent to overcome the limitations of chemotherapy. Herein, we first report a new porous biodegradable nitrogen containing COF material, EDTFP-1 (ethylenedianiline-triformyl phloroglucinol), synthesized using 4,4'-ethylenedianiline and 2,4,6-triformylphloroglucinol via Schiff base condensation reaction. EDTFP-1 exhibited 3D-hexagonal porous structure with average pores of *ca.* 1.5 nm dimension. Here, we have explored the anti-cancer potentiality of EDTFP-1. Result demonstrated an enhanced cytotoxicity was observed against four cancer cells HCT 116, HepG2, A549, and MIA-Paca2 with significant lower IC_{50} on HCT116 cells. Additionally, EDTFP-1-induced cell death was associated with the characteristic apoptotic changes like cell membrane

blebbing, nuclear DNA fragmentation, externalization of phosphatidylserine from the cell membrane followed by a loss of mitochondrial membrane potential as well as modulation of pro and anti-apoptotic proteins. Further, the result depicted a direct correlation between the generations of ROS with mitochondrial-dependant apoptosis through the involvement of p53 phosphorylation upon EDTFP-1 induction, suggesting this COF material is a novel chemotherapeutic agent for cancer treatment.

KEYWORDS: Covalent organic framework, apoptosis, polyphenolic porous framework, anticancer activity, ROS.

1. INTRODUCTION

Cancer is a major global problem and leading causes of mortality.[1] In a recent study conducted to understand the epidemiology of cancer showing an increased death rate of about 8.2 million and 14.1 million of new cases along with the 32.6 million people suffering and living with cancer according to the global follow-up report (GLOBOCAN 2012).[2] In developed countries, lung cancer in male and breast cancer in the female population are among the leading causes of cancer-mortality. The statistics not only shows the gravity of the situation but the increasing trend of the disease is like a step ladder. Extensive researches are being carried out to find a cure through a full spectrum of ailment pathogenicity,[3,4] but the involvement of several organs has made it harder to find a definitive cure till now.[5] Although the conventional chemotherapeutic drugs used nowadays can decelerate the tumor cell growths to a certain extent, cost involved in the treatment, serious life threatening adverse effect and disruption of cellular equilibrium have motivated researchers to enlighten alternative way of effective treatment. To overcome the limitations of the current chemotherapy researchers are always exploring new compounds/materials having anticancer activity.[6,7]

To explore the porous organic materials in nanotechnology, a wide range of COFs[8-10] were synthesized through polymerization of biological building blocks *i.e.* enamine, imine, azine, hydrazine, β-ketoenamine, and boronate esters, bearing strong dynamic covalent bond with a pre-scripted nano-architectures.[11] Due to the periodicity of the porous network, these materials have potential over related conjugated microporous polymers (CMPs),[12] covalent triazine frameworks (CTFs),[13] and porous organic polymers (POPs).[14-17] Further, inherent properties such as large accessible pore size, specific surface area, channel type-ordered structure, low density, crystallinity and high thermal stability are also important factors which can offer a unique advantage over metal organic frameworks (MOFs). [18] Other COFs, eolites,[19] functionalized mesoporous materials[20]and other porous graphene nanocomposites[21] can also be used for biomedical applications as they are devoid of harmful/hydrolyzable metal/metal oxides. Thus, its specific features are desirable to cellular biology (e.g. nano cargo for cancer therapy and imaging)[22] and chemical industry (e.g. heterogeneous catalysis,[23] gas storage,[24,25] proton conduction,[26] Li-storage,[27] photo responsive material[28] and so on). Due to high internal void space, COFs can be treated as nano-carriers in some biomedical applications such as enzyme immobilization and drug delivery.[29] Further, porous biomaterials bearing polyphenolic moieties in their framework are known for their theranostic potential in anticancer research.[30]

Recent advancement in molecular and cell biology suggested that apoptosis[31] is an efficient regulator of cellular homeostasis.[32] Cell death can be achieved through apoptosis which bears characteristic features like nuclear DNA fragmentation, chromatin condensation, membrane blebbing following the cell shrinkage and modulation of pro- and anti-apoptotic factors. There are two families of genes located in DNA; one promotes pro-apoptotic proteins (e.g. p^{53}, Rb, Bad, Bim, Bid, PUMA, and NOXA) and another that inhibits apoptosis activates

anti-apoptotic proteins (Bcl-2/Bcl-XL). Numerous reports revealed that apoptosis is triggered by the DNA damage-sensitive protein, p53, a redox-regulated transcription factor which transcribes plethora of genes that are essential for apoptosis induction.[33-35] Apoptosis is regulated by two signaling pathways, viz extrinsic (cytoplasmic) and another is intrinsic (mitochondrial). It is characterized by a gradual change in mitochondrial membrane potential followed by an alteration of Bax/Bcl2 ratio as well as an increased release of Cytochrome-c which ultimately triggers the cleavage of caspase 3/9.[36-38] Reactive oxygen species (ROS) plays an important role in triggereing a wide spectrum of celluar signaling system and act as a intra and extrac-cellular second massenger to initiate apoptosis mechanism.[39] The balance ROS in physiological system is decisive for maintaining normal cell functions and any interference in the homeostatic balance leads to oxidative stress associated with a wide range of human disorders such as cancers and other associated inflammatory disorders. Thus, induction of apoptosis in cancer cells by any compound/materials can open a new therapeutic window for the nanobiotechnological approach. The above incidents have motivated us to explore the anticancer activity of a novel COF material EDTFP-1 and to develop a molecular mechanism involved in the process. In this study we have demonstrated that porous polymer EDTFP-1 acts as an apoptotic inducer in an *in vitro* system by enhancing the DNA fragmentation, altering the mitochondrial membrane potential and a significant change in apoptotic factors.

2. EXPERIMENTAL SECTION

2.1. Chemicals. 4,4'-Ethylenedianiline (M = 212.29 g/mol), phloroglucinol (M = 126.11 g/mol) and hexamine (M = 140.18 g/mol) were procured from Sigma Aldrich, St. Louis, Missouri, USA. Trifluoroacetic acid (99.5%) was obtained from Alfa Aesar. Hydrochloric acid (HCl) and anhydrous dimethylformamide (DMF) was used without further purification.

2.2. Instrumentation. A Bruker D8 Advance SWAX diffractometer using a fixed voltage (40 kV) and current (40 mA) was employed to get the powder X-ray diffraction patterns of the EDTFP-1 samples. The XRD machine was calibrated with a conventional silicon source employing Ni-filtered Cu Kα radiation with λ=0.15406 nm. Quantachrome Autosorb 1-C surface area analyzer was employed for the nitrogen adsorption/desorption analysis at 77 K. Before the gas adsorption; briefly, the sample was initially degassed for 12 h at 403 K under high vacuum. NLDFT pore size distributions were determined from the N_2 sorption isotherm using the silica/cylindrical pore model. For TEM analysis, 10 mg of the EDTFP-1 sample was dispersed into absolute ethanol for 5 min. under sonication and this is followed by the coating of the sample on a copper grid followed by drying in air before analysis. In order to analyze the morphology as well as the particle size of the EDTFP-1 samples, JEOL JEM 6700 field emission-scanning electron microscope (FE SEM) was used. A series of high throughput biophysical spectral analysis mainly, FT-IR (Nicolet MAGNA-FT IR 750 spectrometer Series II), UV-visible diffuse reflectance spectroscopy (UV 2401PC), and ^{13}C CP MAS NMR spectroscopic analysis (Bruker Advance 500 MHz NMR) of the samples were carried out. A TA Instruments thermal analyzer TA-SDT Q-600 was employed for the thermogravimetric (TG) and differential thermal analysis (DTA) of of EDTFP-1 under air flow with a temperature ranp of 10ºC/min. A Vario EL III CHNOS elemental analyzer was employed for the determination of carbon, hydrogen, and nitrogen contents in the EDTFP-1 material. Additionally, ^{1}H, together with ^{13}C NMR spectra of the TFP monomer were taken on a Bruker DPX-300/500 NMR spectrometer. To check the stability of this COF in water we have treated 100 mg each of the EDTFP-1 samples with three aqueous buffer solutions of pH= 5.5, 7.0 and 7.4. After these water treatments the nanostructure and compositions the samples were analyzed by XRD, FE SEM and

FT IR spectroscopy. Weight of EDTFP-1 samples after pH treatments were 99, 98 and 98 mgs for the solution pH of 5.5, 7.0 and 7.4, respectively. Further, particle size distributions in these aqueous dispersions were analyzed through dynamic light scattering (DLS) experiment by using a Malvern, UK made Malvern zetasizer nano zs 90.

2.3. Synthesis of EDTFP-1. At first 2,4,6-triformylphloroglucinol (TFP) was synthesized following a previously described protocol.[40] Briefly, phloroglucinol and trifluoroacetic acid were mixed up with 250 mL round bottom flask containing hexamethylenetetramine. The solution mixture was stirring in preheated (100°C) oil bath for 2 h under inert atmosphere. Then HCl was added to reaction mixture very slowly with vigorous stirring at same temperature for another 1 h followed by a filtration in the cold celite bed. The filtrate part was subjected to extraction with dichloromethane for four times, and anhydrous sodium sulfate was used to soak moisture. After solvent evaporation using rotary evaporator, the off-white colored fluffy product was obtained and characterized by FTIR, ^{1}H NMR, and ^{13}C NMR spectroscopic techniques.

For a typical synthesis of EDTFP-1, 210 mg (1 mmol) of TFP was dissolved in a cleaned two neck round bottom flask containing anhydrous DMF (10 mL). Then the solution of 4,4'-ethylenedianiline in anhydrous DMF was injected into the above solution using a syringe. The resulting solution mixture was kept in reflux condition under nitrogen containing atmosphere at 150ºC for about 12 h to get the golden yellow colored solid product following a vigorous filtration and thoroughly washing with DMF as well as ethanol for several times to get rid of unreacted organic compounds. An advanced soxhlet extraction was employed to remove the impurity from the surface of the material where methanol was used as a washing solvent. Finally, the material was dried in 75 ºC oven for 2 h, and the resulting COF was designated as EDTFP-1 (Figure 1A). To elucidate the structure of the COF and to calculate the unit cell parameters,

possible 2D models were optimized using the Material studio.[41] Several stacking possibilities were considered following the reported literature data.

2.4. Cell lines and Chemicals. Human hepatocellular carcinoma (Hep G2), Human colorectal carcinoma (HCT 116), Human small lung carcinoma (A549), and Human pancreatic carcinoma (MIA PaCa-2) cell lines were procured from National Centre for Cell Sciences (NCCS), Pune, India. Components of cell culture media viz. Dulbecco's Modified Eagle Medium (DMEM), Penicillin-Streptomycin-neomycin (PSN) antibiotic cocktail, Fetal bovine serum (FBS), trypsin and ethylenediaminetetraacetic acid (EDTA) were obtained from Gibco (Grand Island, NY, USA). Other raw and fine chemicals were purchased from Sisco Research Laboratories (SRL), Mumbai, India and Sigma-Aldrich, St. Louis, Missouri, USA, respectively. Antibodies were bought from Santa Cruz Biotechnology, Dallas, Texas, USA and eBioscience, San Diego, USA.

2.5. Cell culture. Briefly, Cells were cultured in DMEM containing 10% fetal bovine serum (FBS) and 1% antibiotic cocktail at 37°C in a humidified condition under constant 5% CO_2. After 75-80% confluency, cells were harvested with trypsin (0.25%), and EDTA (0.52 mM) in phosphate buffered saline (PBS) and plated at a necessary density to allow them to re-equilibrate before the experimentation.

2.6. Cell Viability. For determining the cell viability, MTT [(4, 5-dimethyl-thiazol-2-yl)-2, 5-diphenyl tetrazolium bromide] assay[42] was carried out to initial screen the cytotoxic effects of EDTFP-1. Cells at required density (2×10^6 cells/well) were seeded in 96 well plate and treated with different concentrations of EDTFP-1 (5, 10, 20, 40, 80 and 100 µg/ml). Soon after treatment, plates were kept in an incubator for 24 hrs at 37 °C in a humidified CO_2-rich condition (5%). After completion of the incubation period, cells were thoroughly washed with PBS followed by the addition of MTT solution (4 mg/ml) and kept it in an incubator for 4 hrs. The

absorbance of the DMSO-solubilized intracellular formazan salt was recorded at 595 nm using an ELISA reader (Emax, Molecular Device, USA). In all cases, the EDTFP-1 samples were sonicated before treating in a cell line to get homogenized mixtures. The final reported biological data were represented after repeating the experiments in triplicate.

2.7. Fluorescence microscopy. For the assessment of chromosomal damage as well as the qualitative discrimination between live and apoptotic cells upon EDTFP-1 treatment, immunofluorescence techniques were obtained through single staining using DAPI (4',6-diamidino-2-phenylindole-dihydrochloride) as well as a combinational staining using acridine orange/ethidium bromide (AO/EtBr). After the treatment, cells were briefly washed with PBS followed by the fixation (3.7% paraformaldehyde) at room temperature for 2 h. The fixed cells were stained with DAPI (10 μg/ml), AO (50 μg/ml), and EtBr (50 μg/ml) before the fluorescence microscopic observation under OLYMPUS IX70 fluorescence microscope (Olympus Optical Co. Ltd., Shibuya-ku, Tokyo, Japan).[43,44] The images were acquired and analysed using Image J software.

2.8. DNA fragmentation assay. Cells were treated with EDTFP-1 at different concentrations (0, 5, 10, 20, 40, 80 and 100 μg/ml) for 24 h and the resultant fragmented DNA was measured using commercially available kits according to the manufacturer protocol.

2.9. Quantification of apoptosis and necrosis using flow cytometry. Determination Apoptosis and necrosis were analyzed by flow cytometry using an Annexin-V FITC/PI apoptosis/necrosis detection kit (Calbiochem, CA, USA).[45] Treated cells (1×10^6) were washed and stained with Annexin-V-FITC and PI in accordance with the manufacturer's instructions. The percentages of viable, apoptotic (early and late) along with necrotic cells were evaluated by flow cytometry (BD LSRFortessa™, San Jose, CA, USA).

2.10. Measurement of mitochondrial membrane potential using flow cytometry. Treated cells were incubated with the cationic carbocyanine dye, JC-1 (5,5′,6,6′-tetrachloro-1, 1′, 3, 3′-tetraethylbenzimidazolylcarbocyanine iodide) followed by flow cytometric analysis according to the manufacturer protocol. JC-1 exhibit potential dependent accumulation in mitochondria and demonstrate a fluorescence emission shift from green (525 nm) to red (590 nm). The fluorescence change, therefore, allows determining the percentage of depolarized and hyperpolarized mitochondria on the basis of the resultant fluorescence of JC-1 monomer and aggregate.[46]

2.11. Determination of intracellular ROS (iROS). Mitochondria are the primary source of the amplification of reactive oxygen species (ROS) production in mammalian cells.[47,48] and it plays a significant role in the stimulation of apoptosis in a variety of cells. To determine the intercellular ROS, the treated cells were incubated with 10 μM of H2DCFH-DA (2′, 7′-dichlorofluorescein diacetate) at 37°C for 25 min before the analysis by flow cytometer (BD LSRFortessa^{TM}, Becton Dickinson, Franklin Lakes, NJ, USA). The increment of DCF fluorescence directly reflects the generated ROS inside cells which were represented as mean fluorescence intensity of DCF. In this experimentation, 2 mM NAC (N-acetyl-cysteine) was also used before 1 h of EDTFP-1 treatment to confirm the ROS-mediated cell death mechanism where it served as a negative control.

2.12. Caspase-3 and caspase-9 activity assays. Treated cells were subjected to caspase-3 and caspase-9 colorimetric assay using commercially available kits according to the manufacturer instruction (BioVision Research Products, Mountain View, CA) respectively.

2.13. Western blot analysis. Immunoblotting is a widely used analytical technique used to identify specific proteins.[49] Briefly, The cell lysate was separated by SDS-PAGE (10–15%)

followed by an optimized transfer to PVDF membranes (Millipore, Bedford, MA). Then the membranes were blocked using 5% bovine serum album (BSA) for 2 h and incubated overnight with respective anti rabbit/mouse primary antibodies (Bcl X_L, Bak, Bim, Noxa, and Puma) at 4°C. β-Actin was used as a loading control. Further, the membrane was washed before the incubation with alkaline phosphatise conjugated secondary antibodies for 2 h at room temperature. Finally, the resultant protein expression was visualized using chromogenic substrates, NBT-BCIP. The intensities of each immunoblot were measured using ImageJ software and represented as mean relative intensities of each protein.

2.14. Assessment of protein expression by flow cytometry. Cells were fixed in paraformaldehyde (4%) in PBS (pH 7.4) for 20 min at room temperature followed by permeabilization (0.1% Triton X-100 in PBS) with 0.1% FBS for 5 min. Then, the permeabilized cells were washed twice using PBS with 3% FBS and incubated with respective anti rabbit/mouse primary antibody for overnight. Further, the primary antibody labeled cells were incubated with FITC-conjugated goat anti-rabbit/mouse IgG as a secondary antibody for 2 h on ice and the stained cells were subjected to flow cytometric analysis using a BD LSRFortessa™ flow cytometer (Becton Dickinson, Franklin Lakes, NJ, USA) equipped with FlowJo software.[50]

2.15. Statistical analysis.

Results were represented as Mean ± SEM of the multiple data points. Statistical significance in the deference was calculated by the analysis of variance (ANOVA) using OriginPro (version 8.0) software where $p<0.05$ was considered as significant.

3. RESULTS AND DISCUSSION

3.1. Powder X-Ray diffraction study. The powder XRD pattern of EDTFP-1 material is shown in Figure 1. The experimentally obtained 2θ values are well matched with the theoretical

simulated powder pattern (Figure 1B) of near-eclipsed stacking model. Hence we propose the structure close to hexagonal space group (*P6/m*) for EDTFP-1 by comparing the experimental and simulated PXRD patterns. As seen from the Figure 1B, the EDTFP-1 displayed three broad peaks below 10 degrees of 2θ, centered at 5.7, 6.6 and 8.7 degrees of 2θ. Further, the observed *d* spacing between the 001 planes was 3.49 Å and this could be attributed to the distance between COF layers due to π–π stacking. An eclipsed structure with the hexagonal space group (P6/m) was constructed by using the Materials Studio software and this result suggested possible 2D hexagonal model for this COF material. The unit cell parameters were: $a = b = 30.5$ Å, $c = 3.49$ Å, $\alpha = \beta = 90.0°$ and $\gamma = 120.0°$. Corresponding unit cell volume was 2813.14 $Å^3$. Ball-stick model corresponding to the optimized crystal structure obtained from this powder XRD data revealed hexagonal crystal structure with unit cells as shown in Figure 1C and 1D.

3.2. Porosity and surface area measurement. The N_2 sorption isotherm of EDTFP-1 (Figure 2) features of both type I and IV isotherms without any hysteresis loop. The significant uptake at relatively low-pressure region (0 to 0.1 P/P_0) represents good microporosity in the polymer matrix together with a steady raise in the N_2 uptake for P/P_0 range of 0.1-0.4 suggested the presence of a broad range of mesopores.[51] The surface area of the material is found to be 223 m^2g^{-1} with a pore volume of 0.107 ccg^{-1}. NLDFT method pore size distribution method was used to understand the size of micropore in EDTFP-1 and this revealed the peak pore width of 1.5 nm. Pore size estimated from the COF crystal structure using Accelrys software agrees very well with this pore width.

3.3. Spectroscopic analysis. ^{13}C CP MAS NMR spectrum of EDTFP-1 (Figure 3) displayed resonance signals at 185, 175, 148, 138, 130, 117, 107, 101 ppm for different carbon atoms present in the polymer framework. The peaks at 185 and 175 ppm originated from the carbonyl

carbon and the carbon atoms present in the aromatic ring in the vicinity of the –N-H bond, respectively. 148 ppm signal is assigned to the enamine carbon atom. The peaks are appeared at 138, 130, 117, 107, 101 ppm corresponding to the different aromatic carbon atoms of the EDTFP-1 framework (Figure 1A). The peak at 107 ppm is observed due to sp^2 carbons of the phloroglucinol moiety. The sharp signal at 38 ppm is assigned due to the presence of ethylene carbon atoms. On the other hand, ^1H and ^{13}C liquid NMR spectra of TFP (Figures S1 and S2) displayed characteristic signals of –CHO groups. The absence of a signal at 192.2 ppm in EDTFP-1 suggested completion of the condensation reaction between TFP and 4,4'-ethylenedianiline. In the FTIR spectrum of EDTFP-1 (Figure 4), a broad peak appeared at 3419 cm^{-1} due to N–H stretching and a weak peak at 1513 cm^{-1} could be assigned due to the N–H bending vibration in the polymer matrix. Further, the presence of two signature peaks centered at 2926 and 2856 cm^{-1} are ascribed for sp^2 and sp^3 hybridized carbon atoms in the organic framework. However, the absence of hydroxyl (–OH) and imine (C=N) stretching bands suggesting that the framework is not present in enol form. The strong FT IR band at 1580 cm^{-1} could be assigned due to the presence of C=C stretching band for enol to keto tautomerization.[52] The characteristic peak in the range of 1244-1294 cm^{-1} was observed for newly formed C–N group. The peak centered at 1622 cm^{-1} could be attributed to the α,β-unsaturated ketone in the polymer matrix in the enol tautomer.[52] Further, the two well-defined peaks were noticed at 3437, and 3372 cm^{-1} for stretching vibration of primary amine (NH_2) group and another strong band at 1619 cm^{-1} due to in-plane bending vibration of NH_2 in 4,4'-ethylenedianiline part was observed (Figure 4c). On the other hand, the UV-visible adsorption band of EDTFP-1 suggested $\pi \rightarrow \pi^*$ and $\sigma \rightarrow \sigma^*$ transitions and the band gap of 2.1 eV (Figure S3).

3.4. Microscopic and thermogravimetric analysis. FE-SEM images of EDTFP-1 (Figure 5) suggested nanofibre like morphology having a diameter of *ca.* 22-30 nm and length of *ca.* 200 nm, and these are randomly distributed throughout the whole specimens to form a bundle of wire like a network. The high-resolution transmission electron microscopic images of EDTFP-1 (Fig. 6a and 6b) further revealed nanofibre type particle morphology with uniform micropores of *ca*.1.5 nm. TGA/DTA plot of EDTFP-1 in air flow (Figure S4) indicated first weight loss due to the desorption of the adsorbed water molecules from the COF, and this is followed by two further weight losss in 310-500 ºC. The latter could be ascribed for the C–C and C–N bond cleavage along with the the burning of remaining organic moieties of polymer framework. Thus, TGA analysis revealed its considerably high thermal stability up to 300 ºC. Further, CHN analysis data showed C= 66.5, H= 4.76 and N= 7.25 %, which agrees very well with the model structure of EDTFP-1 illustrated in Figure 1A.

3.5. *In vitro* drug release. The *in vitro* drug release experiments were conducted at different pHs 5.5 and 7.4 with 10 µg/ml of EDTFP-1 loaded into a dialysis bag. 0.01 mg of EDTFP-1 was dispersed in a known amount (1 ml) of PBS of 7.4 and 5.5 solutions, transferred to dialysis bag and kept at 37ºC. The resulting suspension was immersed into 10 ml of PBS and pH 5.5 solutions and incubated at 130 rpm for a definite time period (4 h 30 min). 500 µl aliquots were drawn from the above dispersions after 30 min intervals, this was replaced by equal volume of the fresh PBS solution and pH 5.5 buffer for retaining the release medium same. EDTFP-1 released amount was studied through the UV spectrophotometic analysis at 420 nm. In Figure 7 we have shown the drug release pharmacokinetics with time on EDTFP-1. The pharmacokinetics plot suggested almost no effect of pH in *in vitro* drug delivery. The drug release was

simultaneously increasing upto 200 min (around 60% of EDTFP-1 COF) and after 200 min it became plateau.

3.6. Chemical stability of EDTFP-1 in water: To understand the stability of the COF material under aquatic conditions in the cells we have treated EDTFP-1 samples after treating at pH = 5.5 (acidic pH), 7.0 (neutral) and 7.4 (PBS buffer) under 1-4 days stirring. We have carried out the DLS studies of the suspended EDTFP-1 particles after treatments at different aqueous buffer solutions. As seen from the DSL studies (Figure 8) with the increase in pH from 5.5 to 7.4 average particle size increases. The increase in the average particle size (length of the nanorods) from 135 nm to 171 nm could be attributed to more favorable aggregation due to deprotonation from mildly acidic to neutral and then to mildly alkaline conditions (as pH increased from 5.5 to 7.4). However, the nanostructure and the composition of the COF remained unaltered as seen from the powder XRD (Figure 8D) and FT IR spectra (Figure 8E), respectively. Weight of the samples before and after water treatments remained almost same, suggested no leaching from the framework. Further, we have sonicated the samples before introducing into the cell line, and the XRD pattern (Figure S6) and FT IR spectrum (Figure 8F) of EDTFP-1 suggested retention of framework bonding of the COF.

Respective FE SEM images of the water treated samples are shown in Figure 9. SEM image analysis suggested that after acidic and neutral pH treatments there is no significant change in particle morphology. However, treatment in PBS buffer at 7.4 the nanofibers are somewhat fragmented to form smaller nanofibers with similar agglomerated particle morphology. To check the stability of this EDTFP-1 COF in water, the sample treated at pH 7.0 for 24 h has been continuously stirred in this condition for another 3 days. This sample after treatment at pH 7.0 for 96 h showed similar nanofiber like morphology. There is no change in

the diameter of the nonofibers after these treatments. This result suggested that EDTFP-1 COF is stable in water, and its composition and structural integrity have been retained after the introduction of this COF into the cell lines. Thus, EDTFP-1 can be internalized into the cells for prolonged period.

3.7. EDTFP-1 induced Apoptosis. Zhang *et al*[53] and Gao *et al*[54] have observed that nanoparticles having radius of ca. 25 nm have the shortest internalization time (20 min.) when they are introduced in cell. The rate of cellular uptake for the nanoparticles reached this optimum limit at this size range as observed Zhang et al. and thus this result suggested that this EDTFP-1 COF can be suitable for intercellular delivery. The EDTFP-1 nanofiber has a particle size of 22-30 nm diameter. So EDTFP-1 can efficiently internalize by endocytosis. The cytotoxic effect of EDTFP-1 was evaluated on A549, HepG2, HCT116 and MIA PaCa-2 cells by MTT assay to determine the cellular death response. Treatment with different concentrations of EDTFP-1 (0 to 100 μg/ml) for 24 h reduced the cell viability significantly and this is dependent on the dose with a lower IC_{50} value of 9.89 ± 1.16 μg/ml for HCT116 and 11.88 ± 1.82 μg/ml for A549 cells when compared with the standard chemotherapeutic drug, 5-fluorouracil (10.24 ± 2.14 μg/ml for HCT116 and 12.30 ± 3.18 μg/ml for A549 cells).[55] On the other hand, the IC_{50} value for EDTFP-1-treated HepG2 (14.38 ± 2.01 μg/ml) and MIA PaCa-2 (14.30 ± 1.32 μg/ml) cells was significantly higher when compared with the 5-fluorouracil-treated cells. Thus, the concentration of 10 μg/ml was selected for the entire experimentation using HCT116 cells. We have checked the cell viability of the monomer units TFP and DEA as controls for HCT116 cell line under controlled experiments. Our experimental results suggested building block monomer units of the COF do not have any activity for inducing apoptosis at 10 μg/mL concentration (Figure S5). These monomers have some cytotoxicity above 40 μg/mL concentration. The dosing amount of

the monomers present in the COF is significantly less than the cytotoxic level. So the monomers do not have any effect at 10 μg/mL concentration in apoptosis.

In order to evaluate whether the cytotoxic effect of EDTFP-1 was directly correlated with apoptosis, morphological analysis of treated cells was determined using immunofluorescence microscopy as apoptotic cells have some characteristic of changes like cell shrinkage, rounding, nuclear condensation and DNA fragmentation.[55] The morphological changes of treated cells (A549 and HCT116) were assessed using AO/EtBr and DAPI staining (nuclear staining dye). The number of dense bright fragmented nuclei was markedly increased in EDTFP-1-treated condition after DAPI staining, and double positive cells ($AO^+/EtBr^+$) were higher in EDTFP-1 treated cells when compared to the untreated control (Figure 10B) as evidenced by yellowish, orange-red or their combination colored nuclei upon AO/EtBr staining. This data was further confirmed by the analysis of DNA fragmentation assay (Figure 10C).

To explore whether the EDTFP-1 was involved in apoptosis/necrosis, flow cytometric assessment was conducted using Annexin-V-FITC/PI staining by studying the exposed level of serine phosphatidyl in the outer membrane of cells. Our result indicated that the % of apoptotic (early and late) cells has been enhanced by time-dependant manner (14.2% EA/14.7% LA for 6 h, 22.3% EA/ 16.3% LA for 12 h and 31.1% EA/4.78% in LA for 24 h) with respect to the control cells (2.66% EA and 0.35% LA) (Figure 10D). These results suggested that EDTFP-1-induced cell death was directly correlated with cytotoxicity followed by apoptosis.

Apoptosis can proceed through the mitochondrial-dependant pathway (intrinsic) or extrinsic pathway (mitochondrial-independent pathway) or both.[56,57] Mitochondria is the power house of cell because of ATP synthesis. A regulated induction of apoptosis has been associated with the mitochondrial dysfunction that suggested to be central to the apoptotic response. That is

why we have shown the mitochondrial membrane potential loss in Figure 10A as a major step of apoptosis signaling pathway. Here we explored whether the EDTFP-1-induced apoptosis in HCT116 cells was involved via the mitochondrial-dependent route, a plethora of indices like loss of mitochondrial membrane potential, changes in the axis of pro-/anti-apoptotic proteins were assessed. Result showed that a significant increase in mitochondrial membrane potential loss in a time-dependent manner (4.74% for 6 h, 8.40% for 12 h and 14.7% for 24 h) due to the enlargement of mitochondrial membrane pore as observed from increased level of JC1 green fluorescence intensity in EDTFP-1 treated cells (Figure 11A). Following death signaling, a significant ($p<0.05$) time-dependent enhancement of Bax and Cytochrome C expressions were found in EDTFP-1-treated cells followed by a marked decrease in Bcl_2 expression when compared with the control cells as seen from the median fluorescence analysis. As we have observed that ROS has been increased by the introduction of EDTFP-1 into the cell there is a subsequent change in Bcl_2 and Bax.. On the other hand, the immunoblot analysis demonstrated a marked ($p<0.05$) time-dependent increase in Bak, Bim, Noxa and Puma expression was found upon EDTFP-1 treatment when compared with the control cells, suggesting that EDTFP-1-induced loss of MMP was correlated with the alteration of pro-and anti-apoptotic protein expression (Figure 11B). FlowJo and Western blot analysis of different apoptosis regulatory proteins are shown in Figures 11C and 11D. The apoptotic fate was also confirmed using caspase 3 and 9 activity assessment in HCT116 cells as the data indicated that EDTFP-1-treatment was significantly augmented caspase 3 and 9 activity concerning the control cells (Figure 11E). The above data suggested that EDTFP-1 treatment triggered the release of pro-apoptotic protein as well as suppress the anti-apoptotic proteins in the mitochondria which were interacted with the increase in caspase activity.[33]

Apoptosis is triggered by elevated ROS either independently or dependently through the p53 phosphorylation.[58] EDTFP-1 is made of phloroglucinol as an integral part of the framework. As reported by Zhang et al the phloroglucinol species present in Dryofragin is responsible for ROS generation inside the cell.[59] In this present study, the level of ROS, p53 expression, and their interplay was analyzed using flow cytometry (Figure 12A and 12B). The mean fluorescence intensity of DCF was significantly ($p<0.05$) increased in a time-dependent manner upon EDTFP-1 treatment. However, the increased level of ROS was markedly suppressed with the pretreatment of standard ROS scavenger, NAC (2 mM). On the other hand, EDTFP-1-treated reduction in cell viability (45.32 ± 1.21) was reversed using NAC (2 mM) treatment (80.35 ± 3.21), and this result suggested that the EDTFP-1-induced cytotoxicity was directly involved with the generation of ROS. To confirm the indirect relation of ROS with the p53 phosphorylation upon EDTFP-1 treatment, flow cytometric analysis was conducted. Figure 9C suggested the time-dependent increase in p53 phosphorylation was significantly suppressed with the treatment of NAC (2 mM) and potent p53 inhibitor, PFT-α (20 μM) as reflected in cell viability analysis. Upon the pre-treatment with PFT-α and NAC on HCT116 cells, the EDTFP-1-induced suppression in cell viability was significantly ($p<0.05$) restored when compared with control cells. Thus, EDTFP-1 induces mitochondrial dependence apoptosis through the modulation of pro- and anti-apoptotic proteins (Figure 13).

4. CONCLUSIONS

We have synthesized a novel microporous covalent organic framework material EDTFP-1 via Schiff base condensation of 4,4'-ethylenedianiline and 2,4,6-triformylphloroglucinol. The porous COF material showed very good BET surface area and 3D-hexagonal crystal structure with abundant polyphenolic network in the polymeric backbone. Our cell culture studies

revealed that EDTFP-1 induced cell death is associated with characteristic apoptotic changes like nuclear condensation, DNA fragmentation, externalization of phosphatidylserine followed by loss of mitochondrial membrane potential, upregulation of pro-apoptotic proteins and downregulation of anti-apoptotic proteins. Thus, EDPTA-1 has huge potential to be employed as an anticancer agent to overcome the epidemiology of cancer in future.

ASSOCIATED CONTENT

Supporting Information

The Supporting Information is available free of charge on the ACS Publications website at DOI: ^{1}H and ^{13}C NMR of TFP, UV-visible spectrum, TG/DTA profile, cell viability tests and powder XRD of EDTFP-1 after sonication (PDF).

AUTHOR INFORMATION

Corresponding Author

*E-mail: msab@iacs.res.in

Author Contributions

The manuscript was written through contributions of all authors. All authors have given approval to the final version of the manuscript. ‡These authors contributed equally.

ACKNOWLEDGMENTS

PB thanks to CSIR, New Delhi for a senior research fellowship. AB wishes to thank DST, New Delhi for instrumental facilities through DST Unit on Nanoscience.

REFERENCES

(1) Schreiber, R. D.; Old, L. J.; Smyth, Mark J. Cancer Immunoediting: Integrating

Immunity's Roles in Cancer Suppression and Promotion. *Science* **2011**, *331*, 1565-1570.

(2) Ferlay, J.; Soerjomataram, I.; Dikshit, R.; Eser, S.; Mathers, C.; Rebelo, M.; Parkin, D. M.; Forman, D.; Bray, F. Cancer Incidence and Mortality Worldwide: Sources, Methods and Major Patterns in GLOBOCAN 2012. *Int. J. Cancer* **2015**, *136,* E359-E386.

(3) Lawrence, M. S.; Stojanov, P.; Mermel, C. H.; Robinson, J. T.; Garraway, L. A.; Golub, T. R.; Meyerson, M.; Gabriel, S. B.; Lander, E. S.; Getz, G. Discovery and saturation analysis of cancer genes across 21 tumour types. *Nature* **2014**, *505*, 495-498.

(4) Nie, F. Q.; Sun, M.; Yang, J. S.; Xie, M.; Xu, T. P.; Xia, R.; Liu, Y. W.; Liu, X. H.; Zhang, E. B.; Lu, K. H.; Shu, Y. Q. Long Noncoding RNA ANRIL Promotes Non-Small Cell Lung Cancer Cell Proliferation and Inhibits Apoptosis by Silencing KLF2 and P21 Expression. *Mol. Cancer Therapeutics* **2015**, *14*, 268-277.

(5) Roos, W. P.; Thomas, A. D.; Kaina, B. DNA damage and the balance between survival and death in cancer biology. *Nature Rev. Cancer* **2016**, *16*, 20-33.

(6) Naksuriya, O.; Okonogi, S.; Schiffelers, R. M.; Hennink, W. E. Curcumin nanoformulations: A review of pharmaceutical properties and preclinical studies and clinical data related to cancer treatment. *Biomaterials* **2014**, *35*, 3365-3383.

(7) Lee, J. E.; Lee, N.; Kim, T.; Kim, J.; Hyeon, T. Multifunctional Mesoporous Silica Nanocomposite Nanoparticles for Theranostic Applications. *Acc. Chem. Res*. **2011**, *44*, 893-902.

(8) Uribe-Romo, F. J.; Doonan, C. J.; Furukawa, H.; Oisaki, K.; Yaghi, O. M. Crystalline Covalent Organic Frameworks with Hydrazone Linkages. *J. Am. Chem. Soc.* **2011**, *133*, 11478-11481.

(9) Ding, S. Y.; Wang, W. Covalent Organic Frameworks (COFs): From Design to Applications. *Chem. Soc. Rev.* **2013**, *42*, 548-568.

(10) Dalapati, S.; Jin, E.; Addicoat, M.; Heine, T.; Jiang, D. L.; Highly Emissive Covalent Organic Frameworks. *J. Am. Chem. Soc.* **2016**, *138*, 5797-5800.

(11) Kandambeth, S.; Venkatesh, V.; Shinde, D. B.; Kumari, S.; Halder, A.; Verma, S.; Banerjee, R. Self-Templated Chemically Stable Hollow Spherical Covalent Organic Framework. *Nature Commun.* **2015**, *6*, 6786.

(12) Xu, Y.; Jin, S.; Xu, H.; Nagai, A.; Jiang, D. L. Conjugated Microporous Polymers: Design, Synthesis and Application. *Chem. Soc. Rev.* **2013**, *42*, 8012-8031.

(13) Kamai, R.; Kamiya, K.; Hashimoto, K.; Nakanishi, S. Oxygen-Tolerant Electrodes with Platinum-Loaded Covalent Triazine Frameworks for the Hydrogen Oxidation Reaction. *Angew. Chem. Int. Ed. Engl.* **2016**, *55*, 13184-13188.

(14) Modak, A.; Nandi, M.; Mondal, J.; Bhaumik, A. Porphyrin Based Porous Organic Polymers: Novel Synthetic Strategy and Exceptionally High CO_2 Adsorption Capacity. *Chem Commun.* **2012**, *48*, 248-250.

(15) Kaur, P.; Hupp, J. T.; Nguyen, S. T. Porous Organic Polymers in Catalysis: Opportunities and Challenges. *ACS Catal*. **2011**, *1*, 819-835.

(16) Zhang, Y. G.; Riduan, S. N. Functional Porous Organic Polymers for Heterogeneous Catalysis. *Chem. Soc. Rev*. **2012**, *41*, 2083-2094.

(17) Zhang, K.; Farha, O. K.; Hupp, J. T.; Nguyen, S. T. Complete Double Epoxidation of Divinylbenzene Using Mn(porphyrin)-Based Porous Organic Polymers. *ACS Catal*. **2015**, *5*, 4859-4866.

(18) An, J.; Farha, O. K.; Hupp, J. T.; Pohl, E.; Yeh, J. I.; Rosi, N. L. Metal-Adeninate Vertices for The Construction of an Exceptionally Porous Metal-Organic Framework. *Nature Commun*. **2012**, *3*, 1618.

(19) Zhang, X.; Liu, D.; Xu, D.; Asahina, S.; Cychosz, K. A.; Agrawal, K. V.; Wahedi, Y. A.; Bhan, A.; Hashimi, S. A.; Terasaki, O.; Thommes, M.; Tsapatsis, M. Synthesis of Self-Pillared Zeolite Nanosheets by Repetitive Branching. *Science* **2012**, *336*, 1684-1687.

(20) Sarkar, K.; Dhara, K.; Nandi, M.; Roy, P.; Bhaumik, A.; Banerjee, P. Selective Zinc(II)-Ion Fluorescence Sensing by a Functionalized Mesoporous Material Covalently Grafted with a Fluorescent Chromophore and Consequent Biological Applications. *Adv. Funct. Mater.* **2009**, *19*, 223-234.

(21) Ali, M. A.; Mondal, K.; Jiao, Y. Y.; Oren, S.; Xu, Z.; Sharma, A.; Dong, L. Microfluidic Immuno-Biochip for Detection of Breast Cancer Biomarkers Using Hierarchical Composite of Porous Graphene and Titanium Dioxide Nanofibers. *ACS Appl. Mater. Interfaces* **2016**, *8*, 20570-20582.

(22) Rengaraj, A.; Puthiaraj, P.; Haldorai, Y.; Heo, N. S.; Hwang, S. K.; Han, Y. K.; Kwon, S. Ahn, W. S.; Huh, Y. S. Porous Covalent Triazine Polymer as a Potential Nanocargo for Cancer Therapy and Imaging. *ACS Appl. Mater. Interfaces* **2016**, *8*, 8947-8955.

(23) Fang, Q.; Gu, S.; Zheng, J.; Zhuang, Z.; Qiu, S.; Yan, Y. 3D Microporous Base-Functionalized Covalent Organic Frameworks for Size-Selective Catalysis. *Angew. Chem. Int. Ed.* **2014**, *53*, 2878-2882.

(24) Gomes, R.; Bhanja, P.; Bhaumik, A. A Triazine-Based Covalent Organic Polymer for Efficient CO_2 Adsorption. *Chem. Commun.* **2015**, *51*, 10050-10053.

(25) Zeng, Y. F.; Zou, R. Q.; Zhao, Y. L. Covalent Organic Frameworks for CO_2 Capture. *Adv. Mater*. **2016**, *28*, 2855-2873.

(26) Xu, H.; Tao, S. S.; Jiang, D. L. Proton Conduction In Crystalline and Porous Covalent Organic Frameworks. *Nat. Mater.* **2016**, *15*, 722-726.

(27) Yang, H.; Zhang, S. L.; Han, L. H.; Zhang, Z.; Xue, Z.; Gao, J.; Li, Y. J.; Huang, C. S.; Yi, Y. P.; Liu, H. B.; Li, Y. L. High Conductive Two-Dimensional Covalent Organic Framework for Lithium Storage with Large Capacity. *ACS Appl. Mater. Interfaces* **2015**, *8*, 5366-5375.

(28) Huang, N.; Ding, X. S.; Kim, J.; Ihee, H.; Jiang, D. L. A Photoresponsive Smart Covalent Organic Framework. *Angew. Chem. Int. Ed.* **2015**, *54*, 8704-8707.

(29) Cui, W.; Li, J. B.; Decher, G. Self-Assembled Smart Nanocarriers for Targeted Drug Delivery. *Adv. Mater*. **2016**, *28*, 1302-1311.

(30) Modak, A.; Barui, A. K.; Patra, C. R.; Bhaumik, A. A Luminescent Nanoporous Hybrid Material Based Drug Delivery System Showing Excellent Theranostics Potential for Cancer. *Chem. Commun.* **2013**, *49*, 7644-7646.

(31) Jiang, T. Y.; Sun, W. J.; Zhu, Q. W.; Burns, N. A.; Khan, S. A.; Mo, R.; Gu, Z. Furin-Mediated Sequential Delivery of Anticancer Cytokine and Small-Molecule Drug Shuttled By Graphene. *Adv. Mater*. **2015**, *27*, 1021-1028.

(32) Poon, I. K. H.; Lucas, C. D.; Rossi, A. G.; Ravichandran, K. S. Apoptotic Cell Clearance: Basic Biology and Therapeutic Potential. *Nat. Rev. Immunol.* **2014**, *14*, 166-180.

(33) Ishikawa, K.; Takenaga, K.; Akimoto, M.; Koshikawa, N.; Yamaguchi, A.; Imanishi, H.; Nakada, K.; Honma, Y.; Hayashi, J. –I. ROS-Generating Mitochondrial DNA Mutations

Can Regulate Tumor Cell Metastasis. *Science* **2008**, *320*, 661-664.

(34) Brentnall, M.; Rodriguez-Menocal, L.; De Guevara, R. L.; Cepero, E.; Boise, L. H. Caspase-9, Caspase-3 and Caspase-7 have Distinct Roles During Intrinsic Apoptosis. *BMC Cell Biol.* **2013**, *14*, 32.

(35) Roos, W. P.; Thomas, A. D.; Kaina, B. DNA Damage and the Balance Between Survival and Death in Cancer Biology. *Nature Rev. Cancer* **2016**, *16*, 20-33.

(36) Arya, R.; Mallik, M.; Lakhotia, S. C. Heat Shock Genes – Integrating Cell Survival and Death. *J. Biosci.* **2007**, *32*, 595-610.

(37) Hu, Q. L.; Gao, M.; Feng, G. X.; Liu, B. Mitochondria-Targeted Cancer Therapy Using a Light-Up Probe with Aggregation-Induced-Emission Characteristics. *Angew. Chem. Int. Ed.* **2014**, *53*, 14225-14229.

(38) de Aberasturi, A. L.; Redrado, M.; Villalba, M.; Larzabal, L.; Pajares, M. J.; Garcia, J.; Evans, S. R.; Garcia-Ros, D.; Bodegas, M. E.; Lopez, L.; Montuenga, L.; Calvo, A. TMPRSS4 Induces Cancer Stem Cell-Like Properties in Lung Cancer Cells And Correlates with ALDH Expression in NSCLC Patients. *Cancer Lett.* **2016**, *370*, 165-176.

(39) Bazhin, A. V.; Philippov, P. P.; Karakhanova, S. Reactive Oxygen Species in Cancer Biology and Anticancer Therapy. *Oxid. Med. Cell Longev.* **2016**, *2016*: 4197815.

(40) Yelamaggad, C. V.; Achalkumar, A. S.; Rao, D. S. S.; Prasad, S. K. Luminescent, Liquid Crystalline Tris(N-salicylideneaniline)s: Synthesis and Characterization. *J. Org. Chem.* **2009**, *74*, 3168-3171.

(41) Accelrys, Material Studio Release Notes, Release 4.2, Accelrys Software, San Diego (**2006**).

(42) Mosmann, T. Rapid Colorimetric Assay for Cellular Growth and Survival: Application to Proliferation and Cytotoxicity Assays. *J. Immunol. Methods* **1983**, *65*, 55-63.

(43) Hamada, S.; Fujita, S. DAPI Staining Improved for Quantitative Cytofluorometry. *Histochem Cell Bio*. **1983**, *95*, 154-157.

(44) Kern, J. C.; Kehrer, J. P. Acrolein-Induced Cell Death: a Caspase-Influenced Decision between Apoptosis and Oncosis/Necrosis. *Chem. Biol. Interact* **2002**, *139*, 79-95.

(45) Dey, S. K.; Bose, D.; Hazra, A.; Naskar, S.; Nandy, A.; Munda, R. N.; Das, S.; Chatterjee, N.; Mondal, N. B.; Banerjee, S.; Saha, K. D., Cytotoxic Activity and Apoptosis-Inducing Potential of Di-Spiropyrrolidino and Di-Spiropyrrolizidino Oxindole Andrographolide Derivatives. *PLOS ONE* **2013,** *8*, e58055.

(46) Nandy, A.; Dey, S. K.; Das, S.; Munda, R. N.; Dinda, J.; Saha, K. D. Gold (I) N-heterocyclic Carbene Complex Inhibits Mouse Melanoma Growth by p53 Upregulation. *Mol. Cancer* **2014**, *13*, 57.

(47) Lambert, A. J.; Brand, M. D. Superoxide Production by NADH:ubiquinone Oxidoreductase (Complex I) Depends on the pH Gradient Across the Mitochondrial Inner Membrane. *Biochem. J.* **2004**, 382, 511-517.

(48) Paravicini, T. M.; Sobey, C. G. Cerebral Vascular Effects of Reactive Oxygen Species: Recent Evidence for a Role of NADPH-oxidase. *Clin. Exp. Pharmacol. Physiol*. **2003**, *30*, 855-859.

(49) Towbin, H.; Staehelin, T.; Gordon, J. Electrophoretic Transfer of Proteins From Polyacrylamide Gels to Nitrocellulose Sheets: Procedure and Some Applications. *Proc. Natl. Acad. Sci*. **1979**, *76*, 4350-4354.

(50) Manna, K.; Das, U.; Das, D.; Kesh, S. B.; Khan, A.; Chakraborty, A.; Dey, S. Naringin Inhibits Gamma Radiation-Induced Oxidative DNA Damage And Inflammation, By Modulating p53 and NF-κB Signaling Pathways in Murine Splenocytes. *Free Radic. Res.* **2015**, *49*, 422-439.

(51) Das, S. K.; Bhunia, M. K.; Sinha, A. K.; Bhaumik, A. Synthesis, Characterization, and Biofuel Application of Mesoporous Zirconium Oxophosphates. *ACS Catal*. **2011**, *1*, 493-501.

(52) Chandra, S.; Kundu, T.; Kandambeth, S.; Babarao, R; Marathe, Y.; Kunjir, S. M.; Banerjee, R. Phosphoric acid loaded azo (-N=N-) based covalent organic framework for proton conduction. *J. Am. Chem. Soc*. **2014**, *136*, 6570-6573.

(53) Zhang, S.; Li, J.; Lykotrafitis, G.; Bao, G.; Suresh, S. Size-Dependent Endocytosis of Nanoparticles. *Adv. Mater.* **2009**, *21*, 419-424.

(54) Gao, H.; Shi, W. D.; Lambert B. F. Mechanics of Receptor-Mediated Endocytosis. *Proc. Natl. Acad. Sci*. **2005**, *102*, 9469-9474.

(55) Focaccetti, C.; Bruno, A.; Magnani, E.; Bartolini, D.; Principi, E.; Dallaglio, K.; Bucci, E. O.; Finzi, G.; Sessa, F.; Noonan, D. M.; Albini, A. Luteolin Inhibits Ischemia /Reperfusion- Induced Myocardial Injury in Rats via Downregulation of MicroRNA-208b-3p. *PLOS ONE* **2015**, *10*, e0115686.

(56) Mallick, A.; More, P.; Ghosh, S.; Chippalkatti, R.; Chopade, B. A.; Lahiri, M.; Basu, S. Dual Drug Conjugated Nanoparticle for Simultaneous Targeting of Mitochondria and Nucleus in Cancer Cells. *ACS Appl. Mater. Interface* **2015**, *7*, 7584-7598.

(57) Liu, B.; Chen, Y.; St Clair, D. K. ROS and p53: A Versatile Partnership. *Free Radic. Biol.*

Med. **2008**, *44*, 1529-1535.

(58) Ly, J. D.; Grubb, D. R.; Lawen, A. The Mitochondrial Membrane Potential (Deltapsi(M)) in Apoptosis; an Update. *Apoptosis* **2003**, *8*, 115-128.

(59) Zhang, Y.; Luo, M.; Zu, Y. G.; Fu, Y. J.; Gu, C. B.; Wang, W.; Yao, L. P.; Efferth, T. Dryofragin, A Phloroglucinol Derivative, Induces Apoptosis in Human Breast Cancer MCF-7 Cells Through ROS-Mediated Mitochondrial Pathway. *Chem-Bio Interactions* **2012**, *199*, 129-136.

Caption for figures

Figure 1 A: Schematic representation for formation of EDTFP-1 COF material. B: Powder XRD pattern of EDTFP-1 (black) and corresponding energy minimized simulated pattern (red). C: Repeating unit cell and D: hexagonal structure of EDTFP-1 COF viewed along pore axis.

Figure 2 Nitrogen adsorption-desorption isotherm of EDTFP-1 material where filled circle and empty circle represents the adsorption and desorption isotherm, respectively. The pore size distribution plot has been shown in the inset of Figure 2.

Figure 3 Solid state ^{13}C CP MAS NMR spectrum of EDTFP-1 material. Different signals are assigned corresponding to the carbon atoms of the framework.

Figure 4 FT IR spectra of EDTFP-1 (a), 4,4'-ethylenedianiline (b) and TFP (c).

Figure 5 FE-SEM images of EDTFP-1 material at two different magnifications: 18000 (a) and 30000 (b).

Figure 6 HR-TEM images of EDTFP-1 material.

Figure 7 *In vitro* time dependent pharmacokinetics of EDTFP-1 drug release at pH of 5.5 and 7.4.

Figure 8 Particle size distribution of EDTFP-1 material estimated from the DLS experiment after treatments at different pHs (A-C). Powder XRD (D) and FT IR (E) spectra of EDTFP-1 after treatments in water at different pHs. FTIR spectrum of EDTFP-1 after sonication for 10 min (F).

Figure 9 FE SEM images of EDTFP-1 after treatments at pH 5.5 (acidic) for 24 h (a), pH 7.0 (neutral) for 24 h (b), pH 7.4 (PBS buffer) for 24 h (c) and pH 7.0 for 96 h (d).

Figure 10 A: Effect of increasing doses (0-100μg/ml) of EDTFP-1 on different cancer cell lines in 24h. B; Morphological and nuclear changes of A549 cells (upper panel) and HCT116 cells (lower panel). Morphological change of normal and EDTFP-1 treated (for 24h) cells (left column of both panels). EtBr/A.O. staining of normal and treated cells (middle column of both panels) for nuclear changes. DAPI staining of normal and treated cells (right column of both panels) for nuclear

changes. C; DNA fragmentation status of A549 and HCT116 cells with increasing doses of the DP. D; Annexin V –FITC /PI positive cells with time of treatment of 10ug/ml of EDTFP-1 by flow cytometry.

Figure 11 A: Change in mitochondrial membrane potential with time following treatment by 10μg/ml of EDTFP-1. B: Level of Bax, Bcl-2 and Cytochrome C positive cells. C: FlowJo analysis of B. D: Western blot analysis of different apoptosis regulatory proteins (left column). Right column is the FlowJo analysis of the same. E: Left column is the level of active caspase-3 and right column is that for Caspase-9 with time of EDTFP-1 (10μg/ml) treated HCT116 cells.

Figure 12 A: Left column is the ROS level with time in 10μg/ml of EDTFP-1 treated cells. Middle column is the level of ROS in presence of ROS inhibitor, NAC (N-acetyl cysteine). Right column is the level of p53 in presence of NAC, pifithrin (PFT-α). B: FlowJo analysis of the results of A. C: Cell viability in presence of NAC, PFT-α with or without the EDTFP-1 (10μg/ml) for 24 h.

Figure 13 Schematic diagram of apoptotic pathway induced by EDTFP-1.

FIGURES

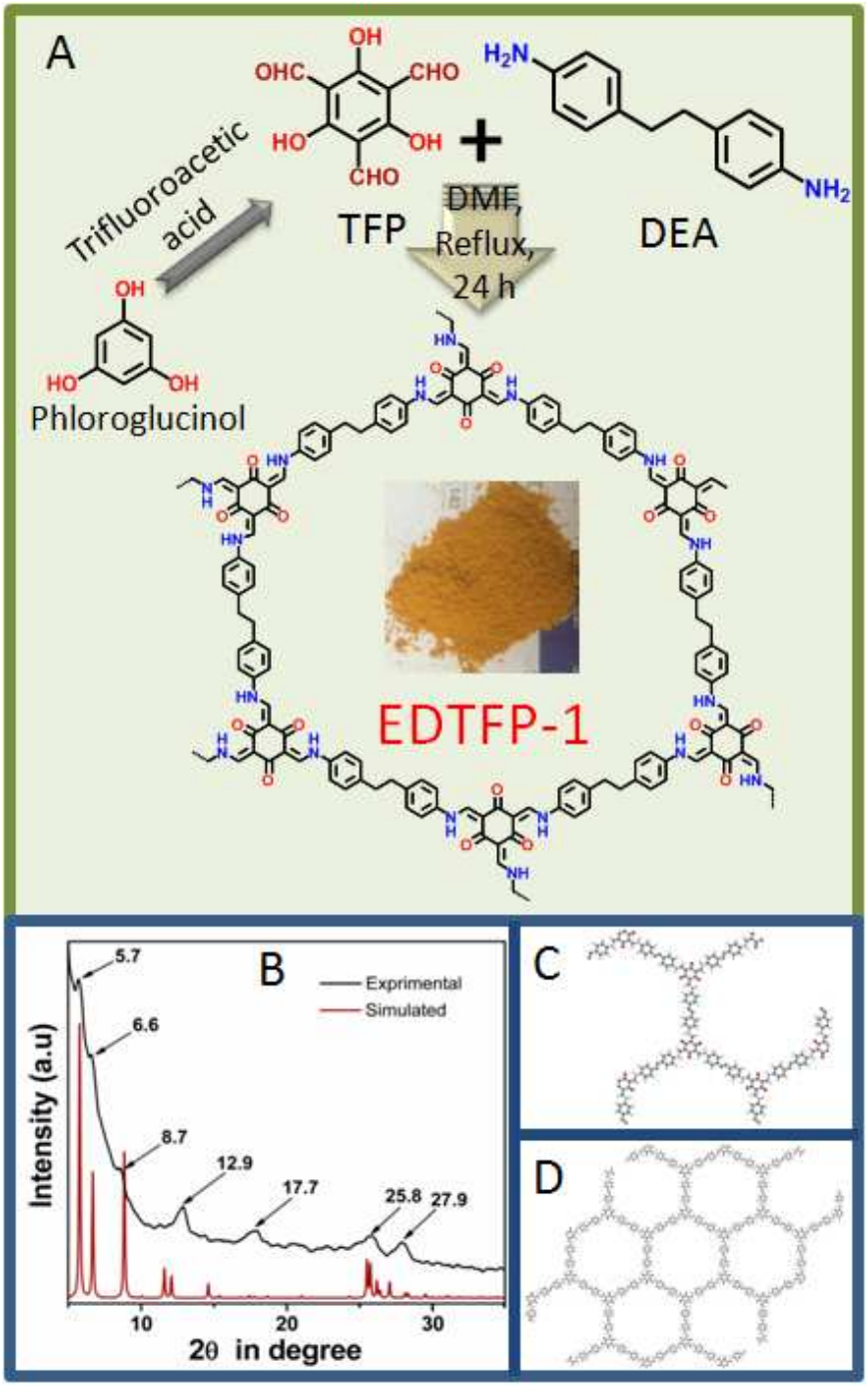

Figure 1. A: Schematic representation for formation of EDTFP-1 COF material. B: Powder XRD pattern of **EDTFP-1** (black) and corresponding energy minimized simulated pattern (red). C: Repeating unit cell and D: hexagonal structure of EDTFP-1 COF viewed along pore axis.

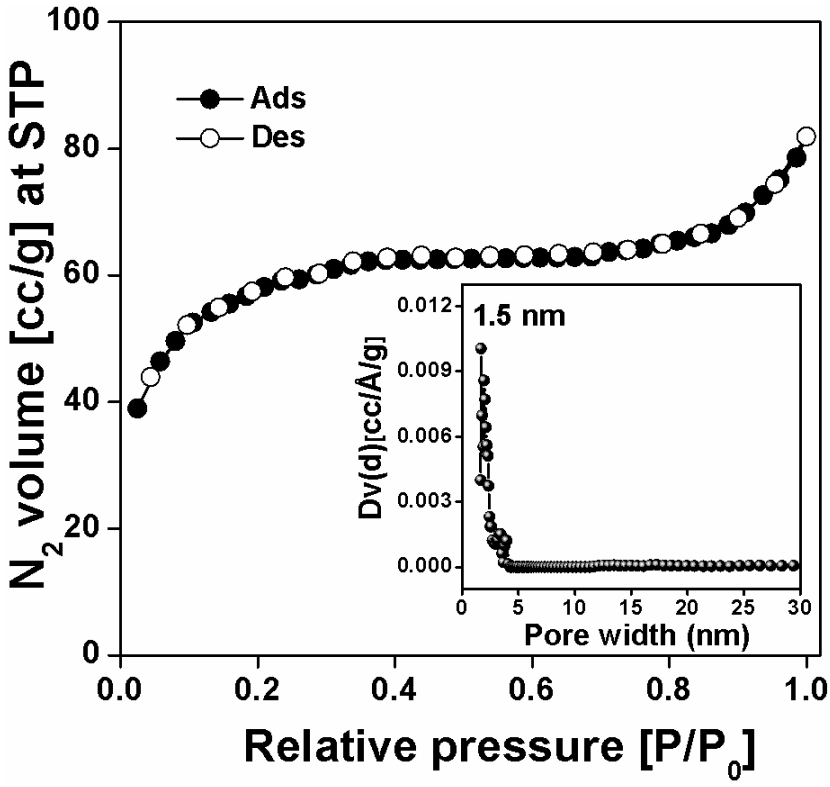

Figure 2. Nitrogen adsorption-desorption isotherm of EDTFP-1 material, where filled circle and empty circle represents the adsorption and desorption isotherm, respectively. The pore size distribution plot has been shown in the inset of Figure 2.

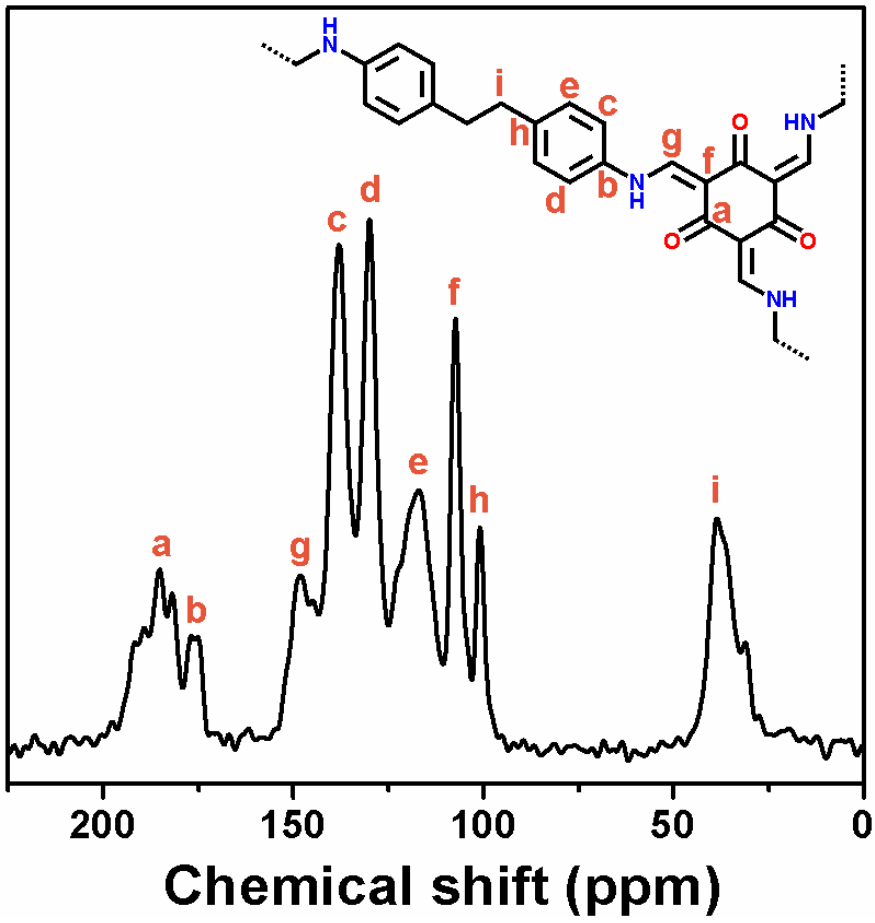

Figure 3. Solid state ^{13}C CP MAS NMR spectrum of EDTFP-1 material. Different signals are assigned corresponding to the carbon atoms of the framework.

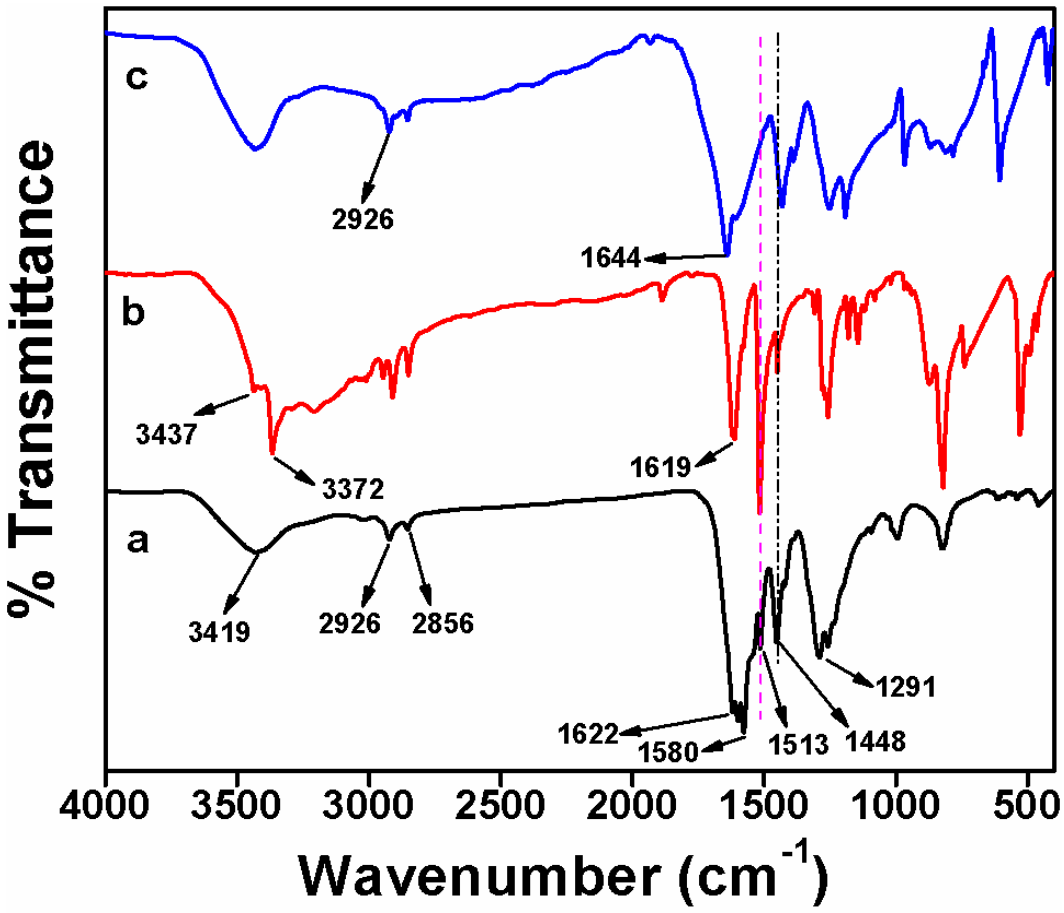

Figure 4. FT IR spectra of EDTFP-1 (a), 4,4'-ethylenedianiline (b) and TFP (c).

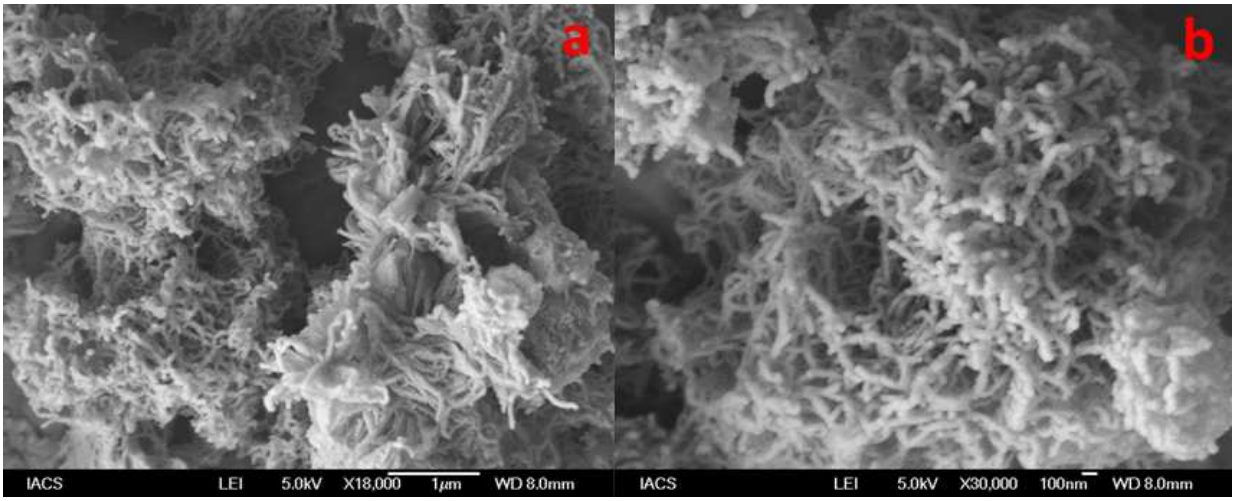

Figure 5. FE-SEM images of EDTFP-1 material at two different magnifications: 18000 (a) and 30000 (b).

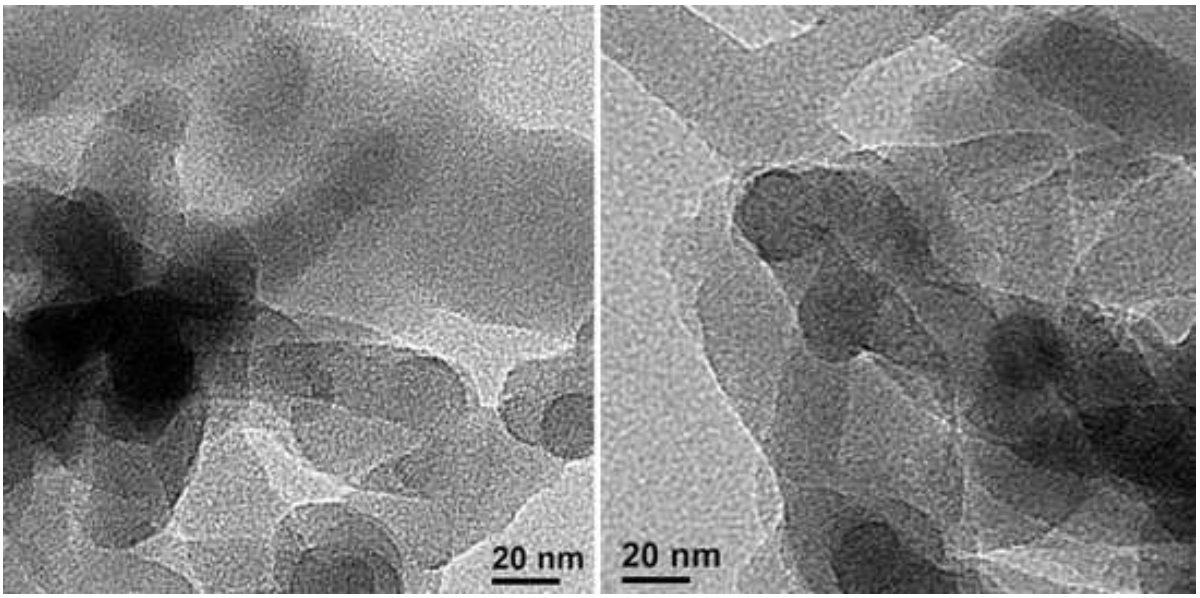

Figure 6. HR-TEM images of EDTFP-1 material.

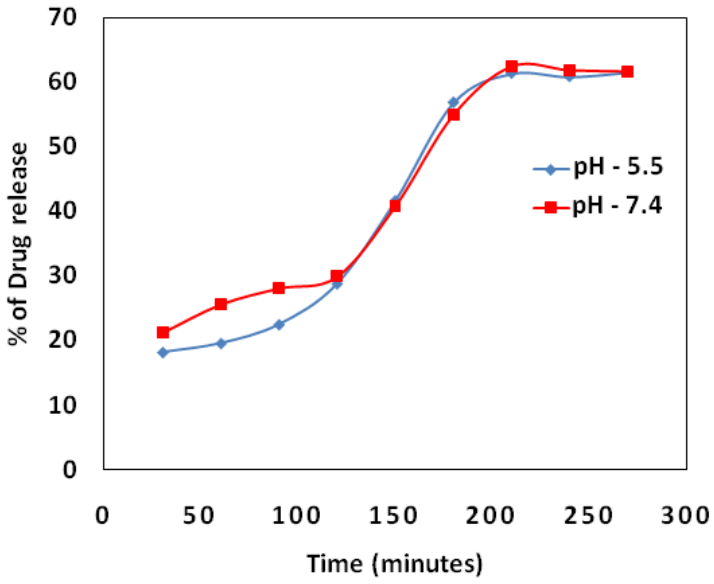

Figure 7. *In vitro* time dependent pharmacokinetics of EDTFP-1 drug release at pH of 5.5 and 7.4.

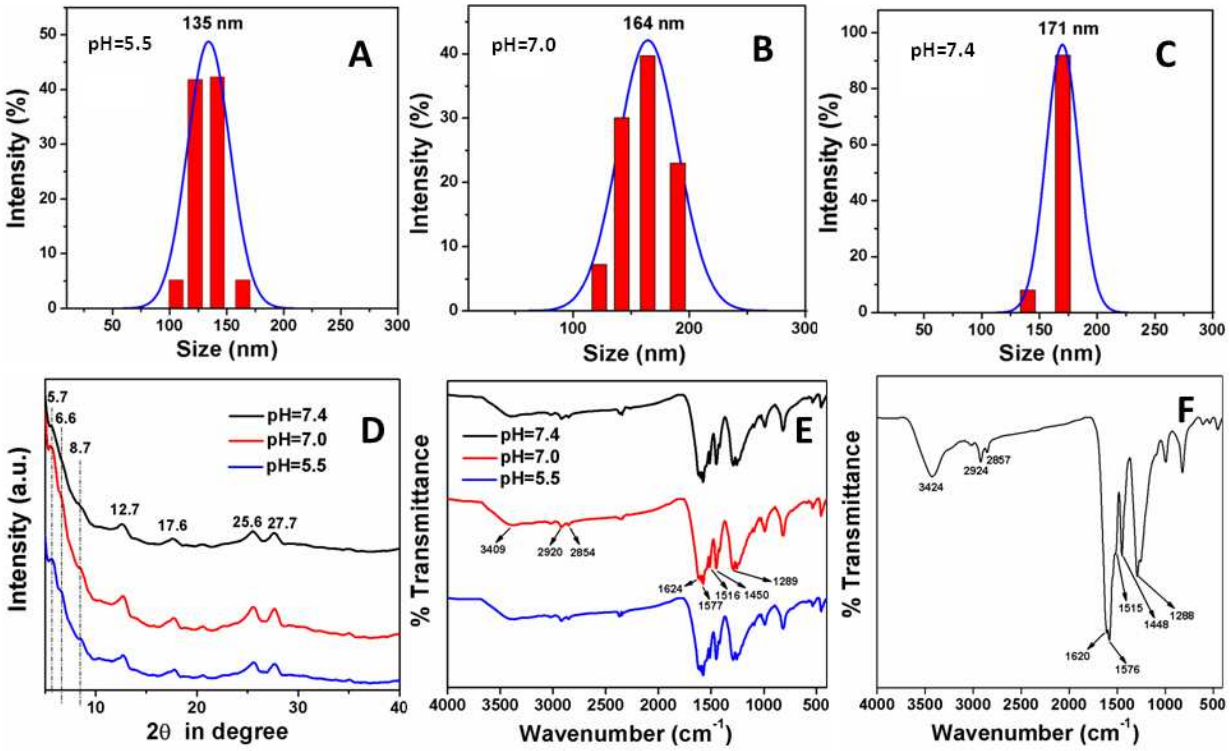

Figure 8. Particle size distribution of EDTFP-1 material estimated from the DLS experiment after treatments at different pHs (A-C). Powder XRD (D) and FT IR (E) spectra of EDTFP-1 after treatments in water at different pHs. FTIR spectrum of EDTFP-1 after sonication for 5 min (F).

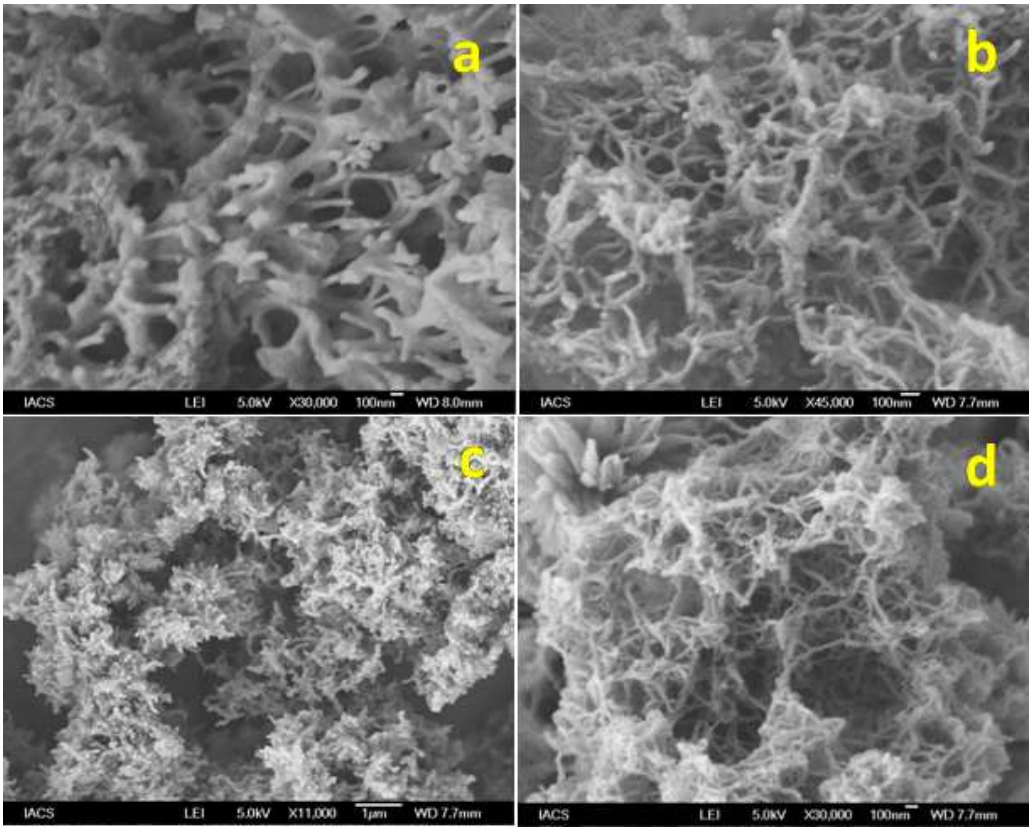

Figure 9. FE SEM images of EDTFP-1 after treatments at pH 5.5 (acidic) for 24 h (a), pH 7.0 (neutral) for 24 h (b), pH 7.4 (PBS buffer) for 24 h (c) and pH 7.0 for 96 h (d).

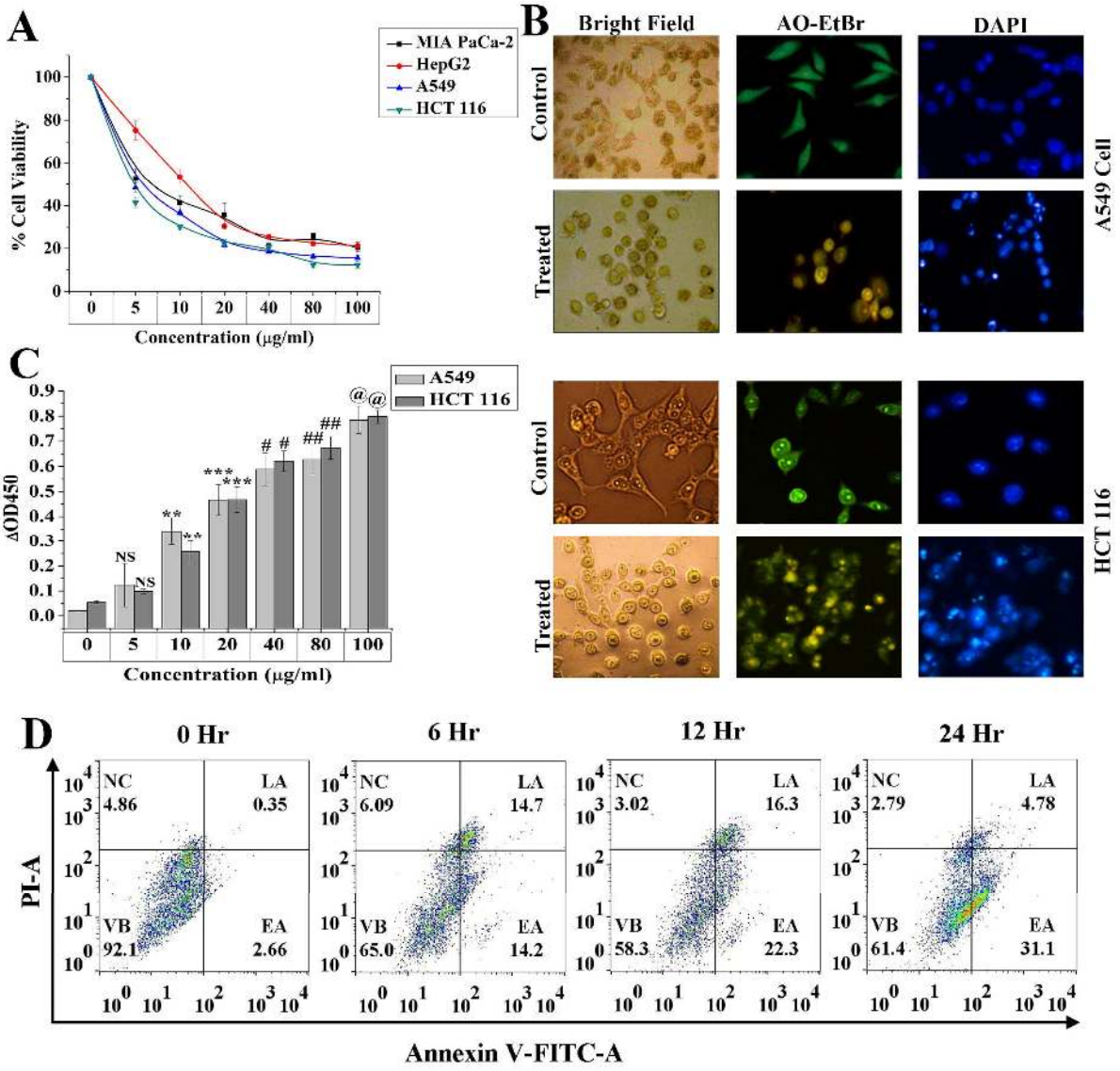

Figure 10. A: Effect of increasing doses (0-100µg/ml) of EDTFP-1 on different cancer cell lines in 24h. B; Morphological and nuclear changes of A549 cells (upper panel) and HCT116 cells (lower panel). Morphological change of normal and EDTFP-1 treated (for 24h) cells (left column of both panels). EtBr/A.O. staining of normal and treated cells (middle column of both panels) for nuclear changes. DAPI staining of normal and treated cells (right column of both panels) for nuclear changes. C; DNA fragmentation status of A549 and HCT116 cells with increasing doses of the DP. D; Annexin V –FITC /PI positive cells with time of treatment of 10ug/ml of EDTFP-1 by flow cytometry.

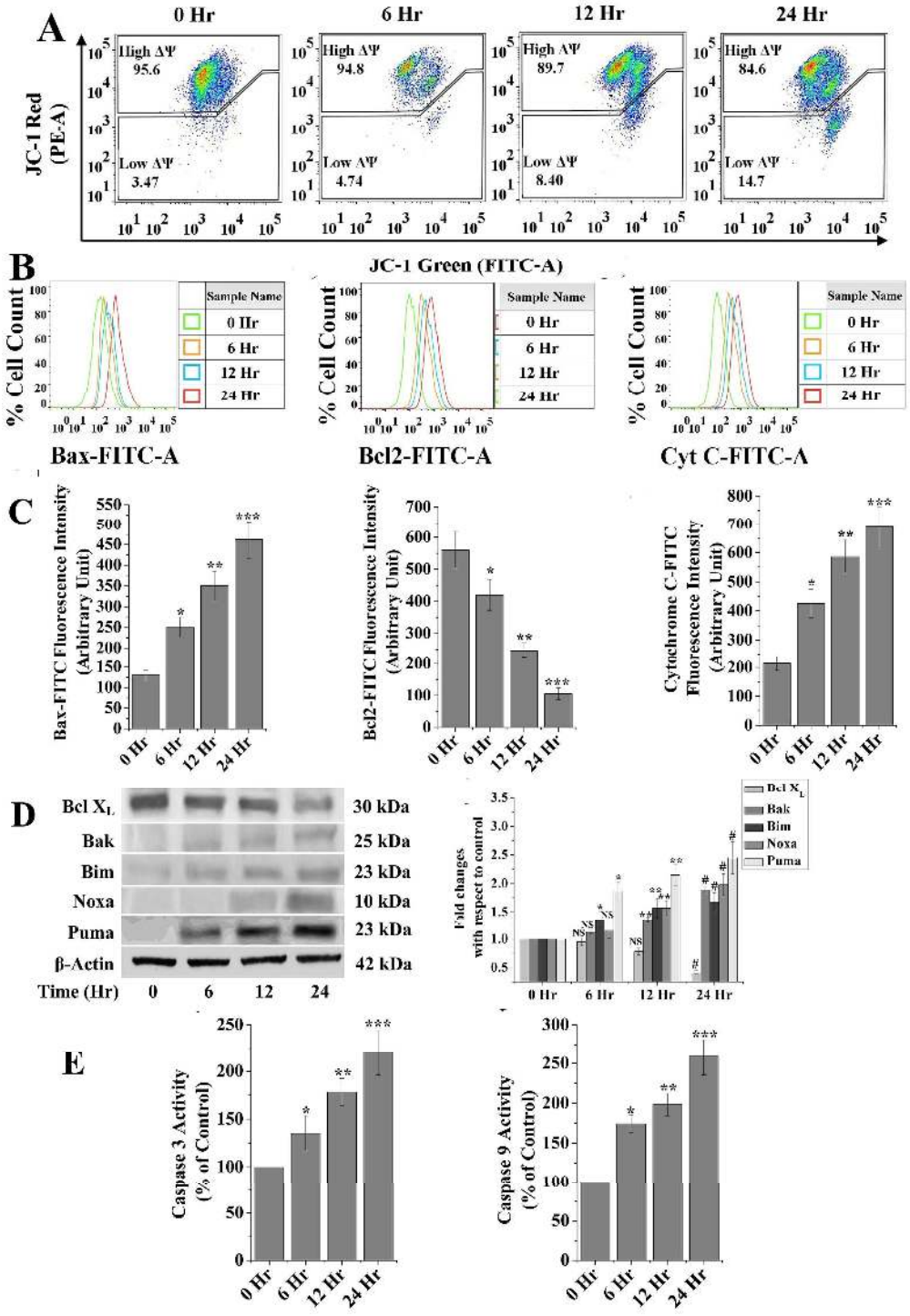

Figure 11. A: Change in mitochondrial membrane potential with time following treatment by 10µg/ml of EDTFP-1. B: Level of Bax, Bcl-2 and Cytochrome C positive cells. C: FlowJo analysis of B. D: Western blot analysis of different apoptosis regulatory proteins (left column). Right column is the FlowJo analysis of the same. E: Left column is the level of active caspase-3 and right column is that for Caspase-9 with time of EDTFP-1 (10µg/ml) treated HCT116 cells.

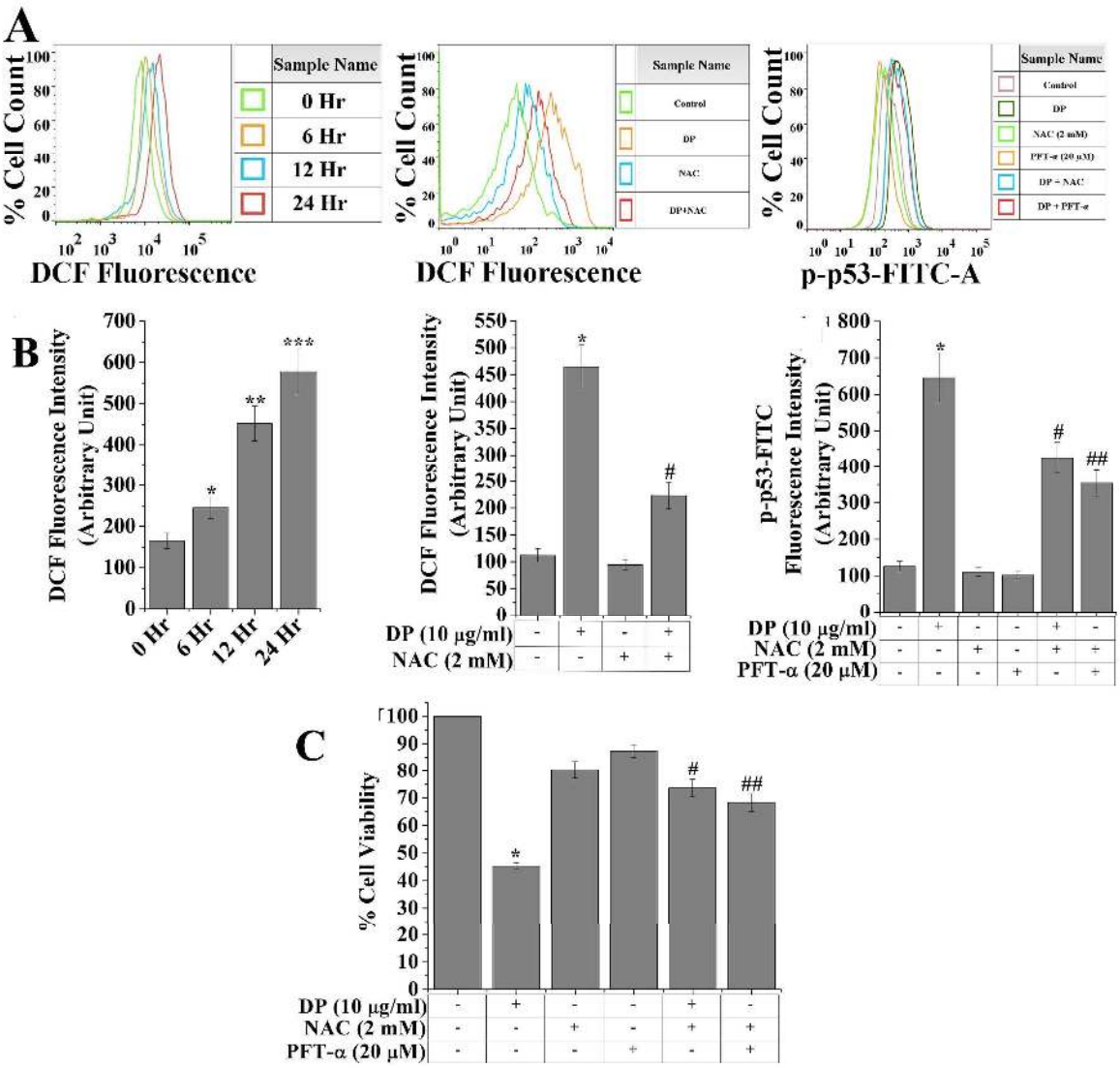

Figure 12. A: Left column is the ROS level with time in 10µg/ml of EDTFP-1 treated cells. Middle column is the level of ROS in presence of ROS inhibitor, NAC (N-acetyl cysteine). Right column is the level of p53 in presence of NAC, pifithrin (PFT-α). B: FlowJo analysis of the results of A. C: Cell viability in presence of NAC, PFT-α with or without the EDTFP-1 (10µg/ml) for 24 h.

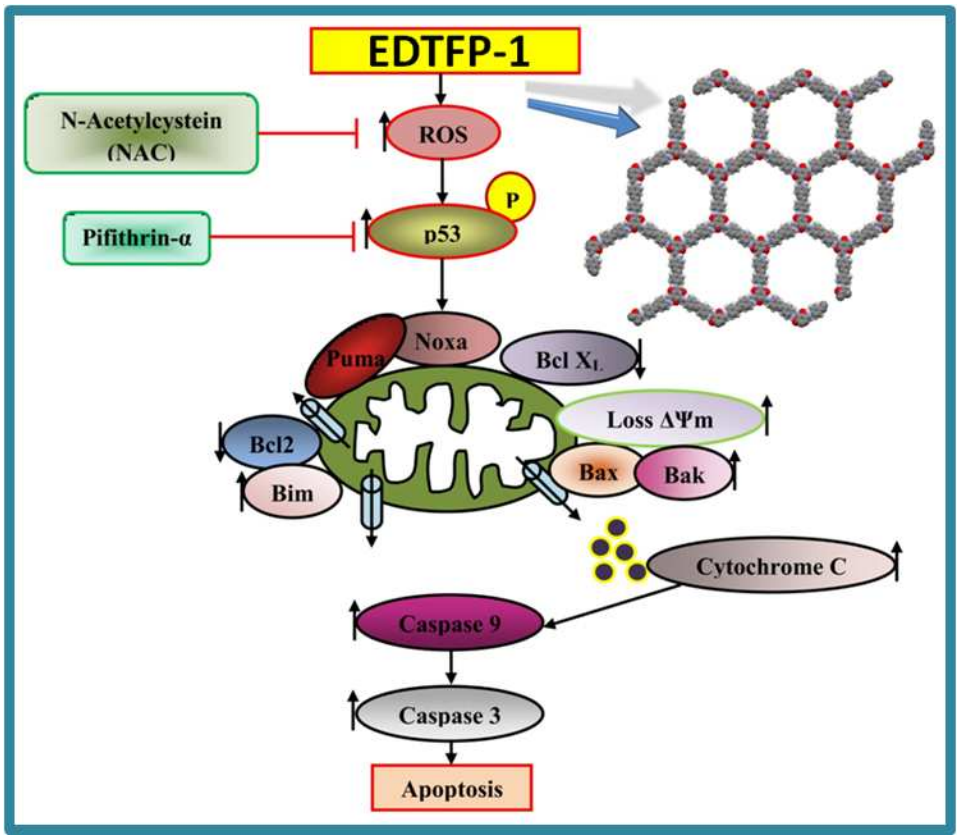

Figure 13. Schematic diagram of apoptotic pathway induced by EDTFP-1.

Table of Contents Graphic